Dry and Wet Snow Cover Mapping in Mountain Areas Using SAR and Optical Remote Sensing Data

Guangjun He, Xuezhi Feng, Pengfeng Xiao, *Member, IEEE*, Zhenghuan Xia, Zuo Wang, Hao Chen, Hui Li,
and Jinjin Guo

***Abstract*—Snow cover in mountain areas is a key factor controlling regional energy balances, hydrological cycle, and water utilization. Optical remote sensing data offer an effective means of mapping snow cover, although their application is limited by solar illumination conditions, conversely, synthetic aperture radar (SAR) offers the ability to measure snow wetness changes in all weather. In this study, a novel method, which can be approached in two steps by using SAR and optical data, has been developed for dry and wet snow cover recognition in mountain areas. First, two ground-based synchronous observations were implemented, respectively, for snow-accumulation period and snow-melt period. Then, the RADARSAT-2 interferometric coherence images and the backscattering coefficient images of the two periods are analyzed, adopting snow-covered and snow-free areas obtained from GF-1 satellite observations as the "ground truth." A dynamic thresholding algorithm was proposed to identify snow cover by taking the polarization mode, local incidence angle, and underlying surface type into consideration. Finally, 36 polarimetric parameters obtained from Pauli, *H/A/*α, Freeman, and Yamaguchi decomposition were analyzed; the results indicate that $P_{\rm vol}$ from Pauli, λ_3 from *H/A/*α, and $Y_{\rm vol}$ from Yamaguchi are more applicable to discriminate dry and wet snow. These three factors, combined with training samples from Nagler algorithm and *in situ* data, were used to build a support vector machine to classify the extracted snow cover to dry and wet snow. The classification results demonstrate that the dry and wet snow cover extraction can achieve an accuracy of 90.3% compared with *in situ* measurements.**

***Index Terms*—Dry snow, interferometric coherence, mountain area, polarimetric decomposition, snow cover mapping, wet snow.**

I. Introduction

SNOW cover is an important component of the cryosphere, and also one of the most active natural elements of the land surface [1], [2]. Seasonal snow cover is the main sources of fresh water resources in arid and semiarid regions of Northwest China. Research on snow cover extraction, especially identifying dry and wet snow, is of great significance to the snow-melt process monitoring, local climate research, snow disaster assessment, and water resources management [3]. Remote sensing can be used to monitor snow cover in large scale and high precision [4]. Especially for the unfavorable weather conditions and rarely meteorological observation in mountain areas, remote sensing is the only effective means of obtaining snow cover information. Optical remote sensing offers an effective way for snow cover extraction in normal situations, but it is difficult to differentiate snow under cloud [5]. In contrast, microwave remote sensing can be used to discriminate snow with other surfaces regardless of weather, time, and solar illumination conditions because of its high penetrability, and also a better sensitivity to snow surface moisture variations. The spatial resolution of current spaceborne passive microwave sensors is too coarse to provide the fine-resolution snow cover data required for snow cover monitoring in mountain areas [6]. Conversely, the spatial resolution of active microwave sensors, particularly synthetic aperture radar (SAR) sensors, is able to provide detailed snow cover information at both the regional and drainage basin scale [7]. Therefore, it can be used to complement optical remote sensing for snow recognition in rugged mountain areas.

Early studies that have used SAR to obtain snow cover information have been carried out using the space shuttle SIR-C/X-SAR. Shi and Dozier evaluated the characteristics of the backscattering, polarization, and frequency ratios of snow in SIR-C/X-SAR images and then developed a supervised classifier based on a classification tree technique [8], [9]. The classifier utilized intensity measurements, polarization properties, and frequency ratios jointly, allowing discrimination between dry and wet snow. However, most of the existing orbital SAR systems are single-frequency types. The regular monitoring of snow cover have become practical after some repeat-pass spaceborne SAR systems, such as the ERS-1, JERS-1, and RADARSAT-1, using a change detection method based on multitemporal and single-polarization images [10]–[12]. Since the backscattering coefficient of C-band co-polarization at a looking angle 40° from wet snow were 10 dB lower than those from dry snow, wet

---

Manuscript received September 14, 2016; revised January 11, 2017; accepted February 10, 2017. Date of publication March 14, 2017; date of current version July 17, 2017. This work was supported in part by the National Natural Science Foundation of China (Grant No. 41671344, 41501379, and 41401377), and in part by the open fund of State Key Laboratory of Space-Ground Integrated Information Technology (Grant No.2016_SGIIT_KFJJ_YG_01). *(The Corresponding author: Pengfeng Xiao.)*

G. He, Z. Xia, and H. Chen are with the State Key Laboratory of Space-Ground Integrated Information Technology, Beijing Institute of Satellite Information Engineering, Beijing 100029, China (e-mail: hgjun_2006@163.com; maxwell_xia@126.com; 824128286@qq.com).

X. Feng, P. Xiao, and J. Guo are with the Department of Geographical Information Sciences, Nanjing University, Nanjing 210023, China (e-mail: xzf@nju.edu.cn; xiaopf@nju.edu.cn; guojinjin95@163.com).

Z. Wang is with the College of Territorial Resources and Tourism, Anhui Normal University, Wuhu 241000, China (e-mail: wzgis2004@163.com).

H. Li is with the Department of Spatial Information Science and Engineering, Xiamen University of Technology, Xiamen 361000, China (e-mail: lih666@163.com).

Color versions of one or more of the figures in this paper are available online at http://ieeexplore.ieee.org.

Digital Object Identifier 10.1109/JSTARS.2017.2673409

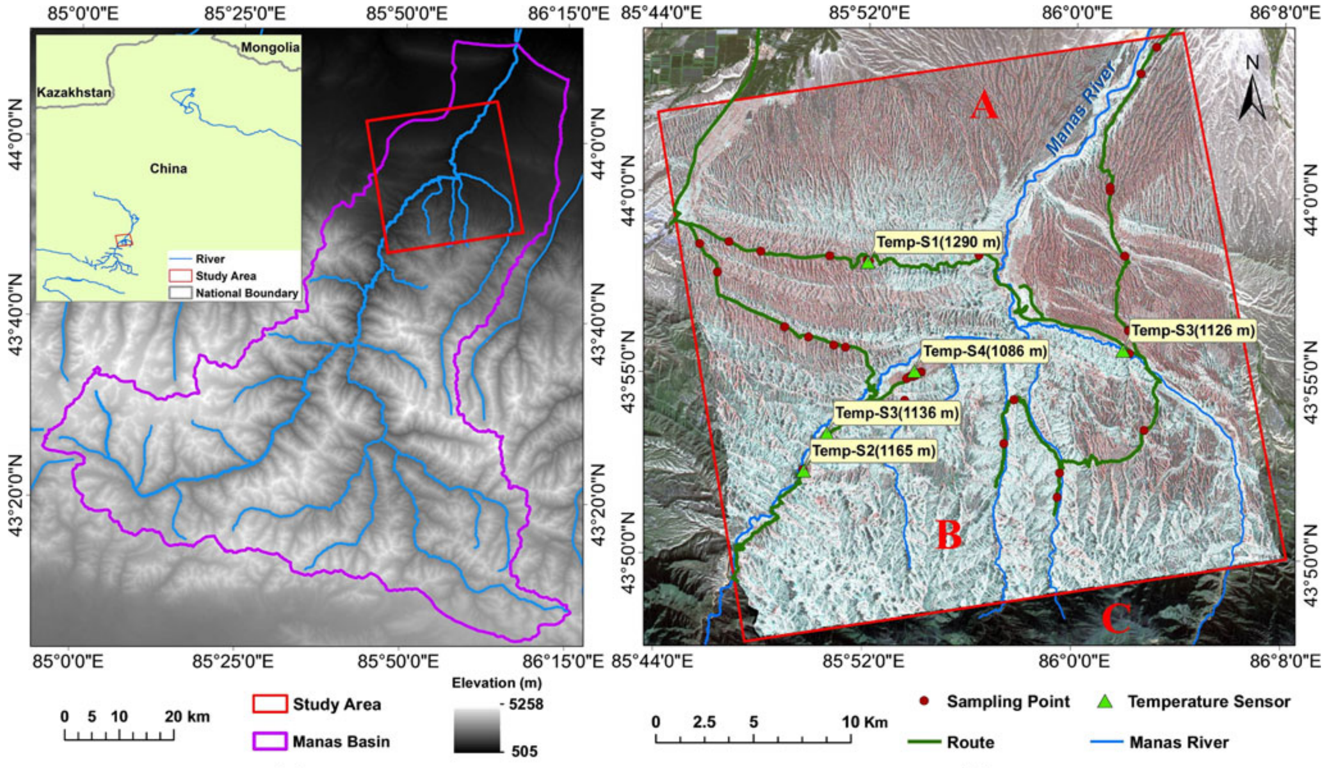

(a) (b)

Fig. 1. Study area. (a) Location of the study area in northwestern China. (b) SAR data of the study area acquired on snow-free period. The red quadrilateral shows the composited image of RADARSAT-2 data with a combination of VV, VH, and HV bands acquired on October 3, 2013. The background image is the WFV data of GF-1 satellite with a combination of green, red, and near-infrared bands acquired on October 2, 2013.

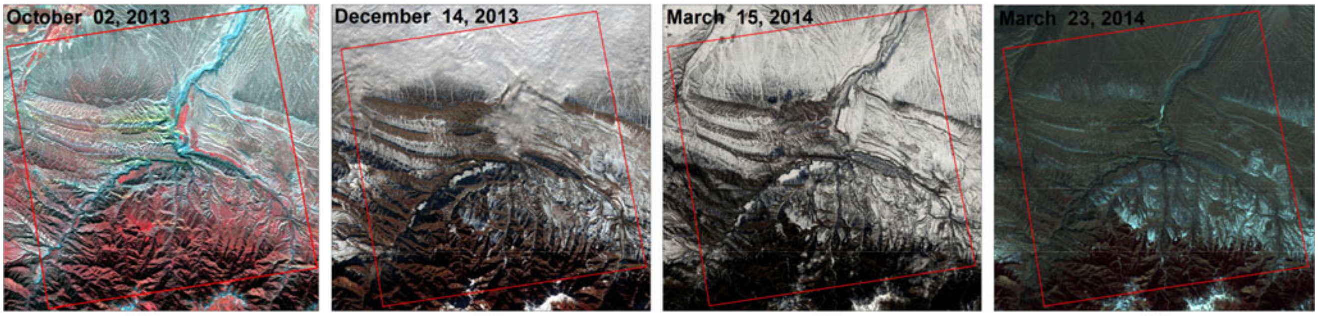

(a) (b) (c) (d)

Fig. 2. Panels (a), (b), and (d) represent the WFV data of GF-1 satellite with a combination of near-infrared, red, and green bands acquired on snow-free period, snow-accumulation period, and snow-melt period, respectively. Panel (c) represents the OLI data of Landsat-8 satellite with a combination of near-infrared, red, and green bands acquired on snow-melt period.

snow cover can be extracted based on the changes in backscattering between a wet snow image and a reference image (either snow free or dry snow) [12]. To overcome the difficulty presented by single frequency and single polarization SAR data, some snow cover mapping methods using the polarimetric SAR data (ENVISAT ASAR, ALOS PALSAR, RADARSAT-2, etc.) have been explored, such as polarimetric decomposition, object based image analysis [13]–[15]. The results showed that polarimetric SAR measurements achieve better classification results than single polarization [16]. Moreover, these studies also indicated that it is not sufficient to detect shallow dry snow using C-band backscattering coefficient images. In brief, the radar penetration depth, which depending on the frequency, can reach more than 10 m for dry snow [17]. The major scattering source at C-band is the snow-ground interface. This makes it difficult to acquire shallow dry snow using backscattering intensity signal of C-band or lower frequencies. However, the measurement of interferometric coherence between two repeat passes offers a way [18]. Since the snow cover has a considerable impact on the interferometric coherence, whereas the snow-free surfaces preserve coherence before and after snowfall, the interferometric coherence of a snow-covered surface is lower than that of a snow-free surface, based on which a threshold slicing algorithm (TSA) has been developed for snow cover extraction [19], [20], although the coherence are severely affected by topography and underlying surface [21].

TABLE I
CHARACTERISTICS OF THE SAR DATA

Satellite	Polarization	Orbit Pass	Incidence Angle	Spatial Resolution (m)	Acquisition Date (YYYY/MM/DD)	Local Time (HH:MM:SS)	Snow Period
RADARSAT-2	Fine Quad-Pol∗	Ascending	43.45°	Range: 12	2013/10/03 (T1)	18:16:51	Snow-free
				Azimuth: 8	2013/12/13 (T2)	18:16:48	Snow-accumulation
					2014/03/19 (T3)	18:16:45	Snow-melt

∗Fine Quad-pol represents combination of four polarization returns: HH, HV, VH, and VV.

TABLE II
CHARACTERISTICS OF THE OPTICAL DATA

Satellite	Sensor	Spectral Band	Wavelength (μm)	Spatial Resolution (m)	Acquisition Date (YYYY/MM/DD)	Cloud Cover
GF-1	Wide Field Viewer (WFV)	Blue	0.450–0.520	16	2013/10/02	< 2%
		Green	0.520–0.590		2013/12/14	>20%
		Red	0.630–0.690		2014/03/23	<2%
		Near Infrared	0.770–0.890			
Landsat-8	Operational Land Imager (OLI)	Green	0.525–0.600	30	2014/03/15	<2%
		Near Infrared	0.845–0.885			
		Short Wavelength Infrared	1.560–1.660			

The objective of the present study is to examine a new method for mapping both dry and wet snow cover in mountain areas using SAR and optical remote sensing data. SAR interferometry and polarimetric decomposition methods were used, respectively, for snow cover extraction and wet snow identification. In considering of practice application and snow characteristics of the study area, snow was divided into two categories, such that below and above 1% (volume water content) are defined, respectively, as dry and wet snow [12], [13].

The paper is organized as follows: The study area and satellite data are described in Section II. In Section III, a brief review of the *in situ* measurements is introduced. Detailed of the methodology are illustrated in Section IV and the results are presented and discussed in Section V. The conclusions are drawn in Section VI.

II. STUDY AREA AND SATELLITE DATA

A. Study Area

An imaging area ($25 \times 25\,\mathrm{km}^2$) of repeat-pass RADARSAT-2 satellite on Quad-Pol mode was selected as the study area. The area falls between latitude 43° 45′ N and 44°05′ N and longitude between 85° 40′ E and 86° 10′ E, and is located in the midstream of the Manasi River Basin on the north slope of the Tianshan Mountains in northwestern China (see Fig. 1). The altitude of the area extending from 714 m in the piedmont slopes (patch A) and up to 3180 m above the spruce forests (patch B). Altitudinal zonation in mountain vegetation characteristics is apparent, with bare land and sparse vegetation in the north, subshrubs and grass in the middle, and alpine meadow and spruce forest in the south. Several glaciers are located in the south side (patch C). The area lies within the seasonal snow cover zone, according to the meteorological statistical data from 1994 to 2013; snow accumulation period in this region extends from November to February in the following year. Typically, snow begins to melt at the end of February or in early March.

B. Satellite Data

In this study, SAR and optical remote sensing data were combined used. Three repeat-pass RADARSAT-2 Fine Quad-Pol single-look complex (SLC) images were subscribed after an overall consideration about the feasibility of *in situ* measurements, temporal and spatial distribution of the snow, and the synchronism of SAR and optical data. In detail, the three SAR images were acquired, respectively, on October 2, 2013 (T1) during snow-free period, December 13, 2013 (T2) during snow-accumulation period, and March 15, 2014 (T3) during snow-melt period. According to the acquisition date of the RADARSAT-2 images, the wide field viewer (WFV) data of GF-1 satellite and operational land imager (OLI) data of Landsat-8 satellite were selected to interpret snow-covered and snow-free samples, and the samples can be used for SAR image analysis, the proposed dynamic thresholding algorithm, and results verification (see Fig. 2). In addition, WFV data acquired on October 2, 2013 represents totally snow-free conditions and was used to obtain the underlying surface information. The WFV sensor is a multispectral scanning radiometer on board the GF-1 satellite of China, launched on April 26, 2013, with a scanning swath of 800 km (four WFV sensors combination) and a temporal resolution of four days. Additional parameters related to the SAR data are listed in Table I and the optical data are listed in Table II. Advanced Spaceborne Thermal Emission and Reflection Radiometer Global Digital Elevation Model (ASTER GDEM) Version 2 product with a spatial resolution of 30 m and vertical accuracy of 17 m at the 95% confidence level [22], was employed for ortho-rectification, radiometric terrain correction, co-registration, and geocoding of SAR and optical data.

III. GROUND-BASED SYNCHRONOUS OBSERVATION

According to the imaging date of the subscribed RADARSAT-2 satellite data, ground-based synchronous observation were implemented during December 10–17, 2014 and March 15–22,

(a) (b)

Fig. 3. *In situ* measurement in snow-melt period. (a) Placement of temperature sensor. (b) Snow wetness measurement.

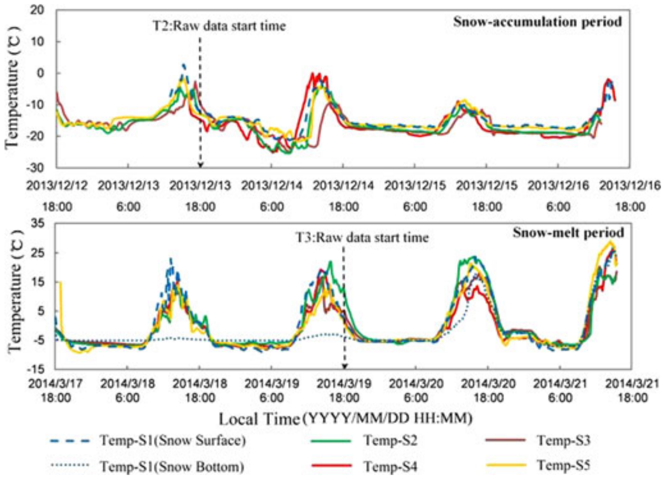

Fig. 4. Changes of snow surface temperature during *in situ* measurements.

2014, respectively, for snow-accumulation period and snow-melt period. Temperature sensors were placed at different elevations [see Fig. 1(b)] to record the snow surface temperature every 10 min, as is shown in Fig. 3(a). Fig. 4 illustrates the changes of snow surface temperature that occurred during the *in situ* measurements. In particular, the snow surface temperature ranges from –25 °C to 0 °C in snow-accumulation period and –10 °C to 30 °C in snow-melt period, which shows a general dry snow state on December 13, 2013 and a snow melting condition on March 19, 2014. There were 34 areas in snow-accumulation period and 31 areas in snow-melt period [see Fig. 1(b)] selected, respectively, to make vertical profiles of snow cover (snow pits). A SnowFork [see Fig. 3(b)] was used to measure the electrical parameters, such as resonant frequency and attenuation, and to calculate the liquid water content [23], According to the measurement results at 2 cm below the snow surface, snow surface wetness are most below 1% on T2 and are between 0% and 7% on T3. The average snow depth is about 25 cm on T2 and 30 cm on T3.

IV. METHODOLOGY

A flowchart summarizing the method proposed in this study is presented in Fig. 5. It includes the following steps: SAR and optical data preprocessing, backscattering coefficient and coherence images analysis, snow cover extraction using dynamic thresholding algorithm, polarimetric decomposition and polarimetric parameter selection, and dry and wet snow classification.

A. Data Preprocessing

1) Preprocessing of SAR images: The RADARSAT-2 SLC images were processed using the SARScape software. Backscattering coefficient and interferometric coherence images are generated, respectively. For the backscattering coefficient images, first, the SLC images were multilooked three times in azimuth and two times in range direction so that the spatial resolution were reduced to 13.764 m × 14.337 m (range × azimuth). Second, a refined Lee filter [24] was used to suppress speckle with window size 5 × 5. Third, the calibration and radiometric terrain correction were conducted with the ASTER GDEM V2 product and the backscattering coefficient images were projected onto the DEM coordinate system. Local incidence angle, shadow/layover images are also generated in the third step. For the coherence images, first, co-registration of the SLC images acquired on different days was performed using a maximum correlation algorithm with the ASTER GDEM V2 product. Then the baseline was estimated by taking the image from October 2, 2013 as the master and December 13, 2013, March 19, 2014 as slave, respectively. The perpendicular baseline (T1–T2, 161.73 m; T1–T3, 37.66 m) were considered to be within the reasonable range. Finally, the interferogram and coherence images were generated.

2) Preprocessing of Optical Images: The optical remote sensing data were used to extract snow-covered and snow-free areas outside the shadow and cloud areas, and to select the samples for SAR image analysis and snow cover extraction using dynamic thresholding algorithm. First, the ortho-rectification and radiometric calibration were conducted using the ENVI software based on the ASTER GDEM V2 product. Second, the Fast Line-of-sight Atmospheric Analysis of Hypercubes (FLAASH) atmospheric correction model was used to process the radiance images to reflectance images. The normalized difference vegetation index (NDVI) [25] was calculated using the reflectance data on October 2, 2013. The normalized difference snow index (NDSI) [26] algorithm was used to mapping the snow cover from the OLI sensor data on March 15, 2014. For lack of the short wavelength infrared band required by NDSI algorithm, the maximum likelihood classification method was adopted to obtain snow-covered and snow-free areas from the reflectance data of WFV sensor on December 14, 2013 and March 23, 2014. The cloud and shadow areas were removed manually to ensure the accuracy of the samples. Finally, all the images were resampled to a pixel spacing of 16 m using the nearest neighbor method.

B. SAR Image Analysis

Backscattering received by SAR antenna from natural snow-covered surface are the sum of surface scattering on the air/snow interface, volume scattering within the snowpack, scattering at the snow/ground interface, and the heterogeneous volumetric scattering from the underlying surface [17]. Therefore, the backscattering intensity depends not only on polarization mode, frequency, and local incidence angle of SAR platform, but also

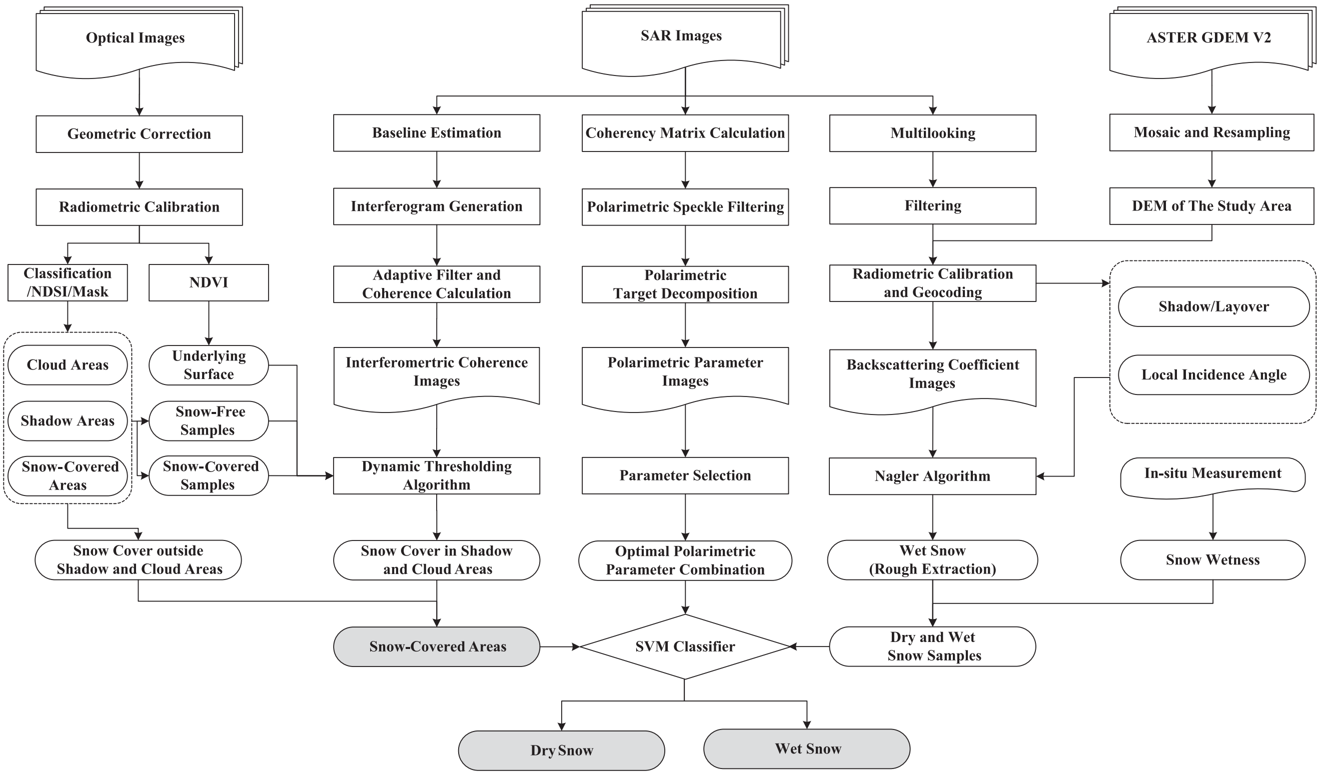

Fig. 5. Flowchart illustrating the method adopted in the study.

the physical characteristics (dielectric constant, surface roughness, etc.) of snow pack and underlying surface. It is difficult to separate the effects of the four parts for shallow snow in rugged high mountain areas.

In order to obtain snow cover information directly from the backscattering coefficient images, the backscattering coefficient value are analyzed. First, the underlying surface was divided into three types: mountain forest (MF) areas, high vegetation coverage (HVC) areas, and low vegetation coverage (LVC) areas, according to the land use map obtained from the land use database of China at a scale of 1:100 000 and the NDVI image on October 2, 2013. The MF areas were not considered in this study owing to the complexity of backscattering. Snow-covered areas obtained from the optical data on December 14, 2013 and March 23, 2014 were selected as snow-covered pixels for December 13, 2013 (T2) and March 19, 2014 (T3), respectively, and snow-free areas obtained from the optical data on December 14, 2013 and March 15, 2014 were selected as snow-free pixels for T2 and T3, respectively. Then the average backscattering coefficient values of selected snow-covered and snow-free pixels were calculated at an interval of 5° for each underlying surface type with local incidence angle in the range 0°–90° (see Fig. 6). In particular, the average backscattering coefficient values of HH and VV polarization is higher than HV and VH polarization on T1, T2, and T3. For the case of the local incidence angle less than 60°, the average backscattering coefficient values of snow-covered pixels were found to be smaller than that of the snow-free pixels, about 2–5 dB on T2, and 5–10 dB on T3. For the case of different underlying surface type, average backscattering coefficient values of LVC areas is about 2–3 dB higher than HVC areas on T1, and approximately equal on T2 and T3 for snow-covered pixels and snow-free pixels. From T2 to T3, the average backscattering coefficient values of the snow-covered pixels decreased obviously, and increase slightly for that of the snow-free pixels in HH, HV, VH, and VV polarization, it may be because the increase of snow wetness and soil moisture, which caused by the rapid melting of snow on T3.

Without considering the effects of the SAR platform and data processing algorithm, for T1–T2 and T1–T3 data pairs, the coherence value is heavily dependent on the two primary factors: underlying surface variation, including snow accumulation, snow melting, underlying surface changes; and local incidence angle, which are related to the topography of mountain areas. In order to investigate the decorrelation caused by the variations of underlying surface, the underlying surface was also divided into the three types described in the previous paragraph.

The MF areas were also not considered in this study owing to the complexity of their decorrelation. To analyze the influence of local incidence angle, the average coherence values of selected snow-covered and snow-free pixels were calculated at an interval of 5° for each underlying surface type with local incidence angle in the range 0°–90°, respectively, for T1–T2 and T1–T3 data pairs (see Fig. 7). Similar to backscattering coefficient, the average coherence values of HH and VV polarization were found to be significantly higher than that of HV and VH polarization. This may be because that the co-polarizations own a higher backscattering intensity in the study area. Owing to the decorrelation caused by snow cover, the average coher-

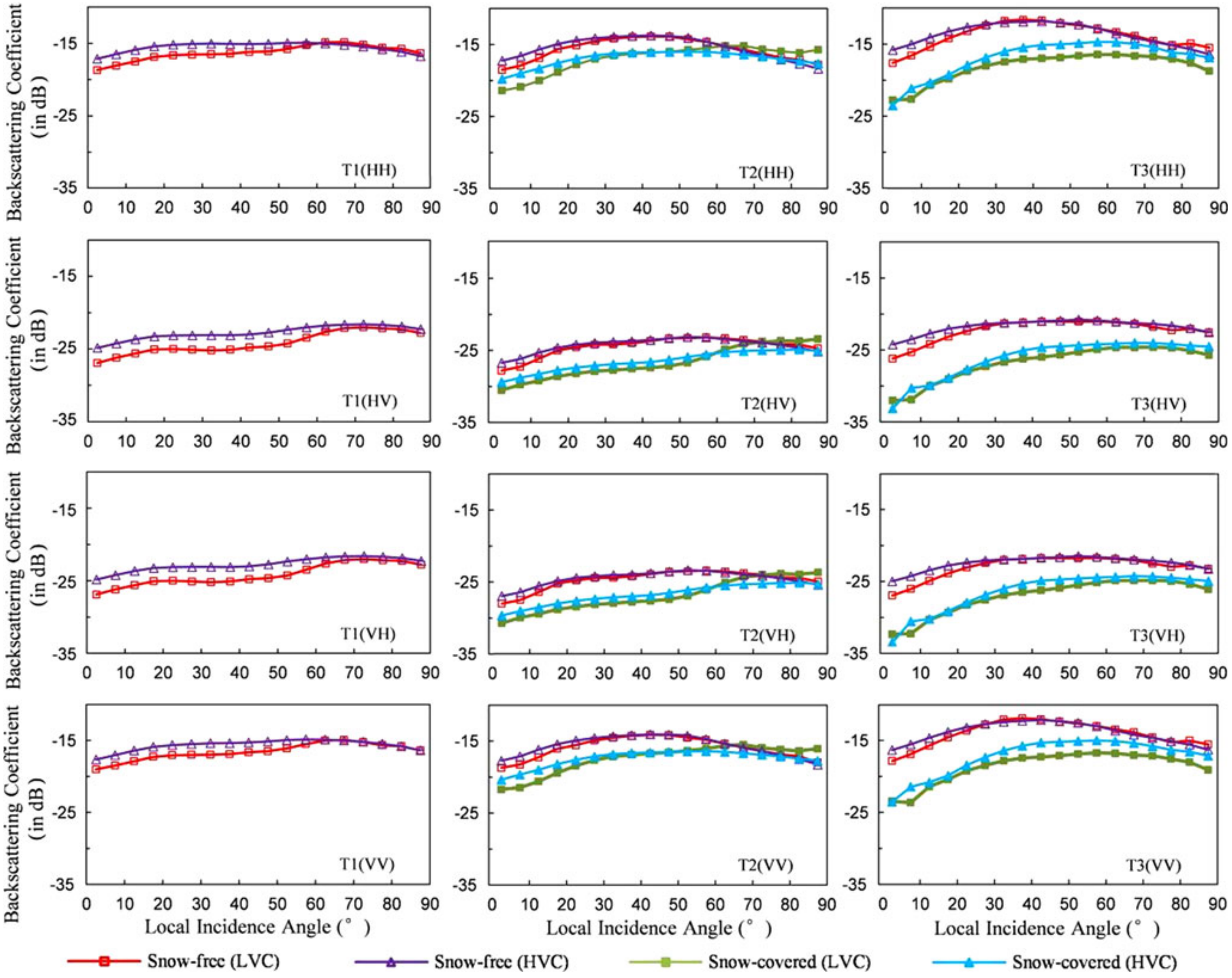

Fig. 6. Backscattering coefficient value comparisons for snow-covered and snow-free pixels from HVC and LVC areas.

ence value of snow-covered areas was found to be smaller than that of snow-free areas, especially in HH and VV polarizations. In particular, the average coherence differences between snow-covered and snow-free pixels in HH and VV polarizations were found to be more significant than those for HV and VH polarizations. For the underlying surface type, the coherence loss of the HVC areas was higher than that of the LVC areas in HH and VV polarizations, and the difference between HV and VH polarizations was not pronounced. Moreover, the average coherence values are clearly correlated to the local incidence angle in HH and VV polarizations, such that the average coherence increases from 0° to 30° and decreases from 40° to 90°. Therefore, polarization mode, local incidence angle, and underlying surface type should be considered when extracting snow cover using coherence images in mountain areas.

C. Polarimetric Information Analysis

As analyzed previously, snow cover can be extracted by the measurement of interferometric coherence. Therefore, in this section, we focus on how to differentiate the wet snow from the snow cover. Pauli decomposition [27] was applied to analyze the polarimetric information of dry and wet snow. Pauli decomposition expresses the scattering matrix S as the complex sum of the Pauli matrices:

$$S = \begin{bmatrix} S_{\mathrm{HH}} & S_{\mathrm{HV}} \\ S_{\mathrm{VH}} & S_{\mathrm{VV}} \end{bmatrix} = \frac{a}{\sqrt{2}}\begin{bmatrix} 1 & 0 \\ 0 & 1 \end{bmatrix} + \frac{b}{\sqrt{2}}\begin{bmatrix} 1 & 0 \\ 0 & -1 \end{bmatrix} + \frac{c}{\sqrt{2}}\begin{bmatrix} 0 & 1 \\ 1 & 0 \end{bmatrix} + \frac{d}{\sqrt{2}}\begin{bmatrix} 0 & -j \\ j & 0 \end{bmatrix} \tag{1}$$

where a, b, c, and d are all complex and are given by

$$a = \frac{S_{\mathrm{HH}} + S_{\mathrm{VV}}}{\sqrt{2}}, \quad b = \frac{S_{\mathrm{HH}} - S_{\mathrm{VV}}}{\sqrt{2}}, \quad c = \frac{S_{\mathrm{HV}} + S_{\mathrm{VH}}}{\sqrt{2}}, \quad d = j\frac{S_{\mathrm{HV}} + S_{\mathrm{VH}}}{\sqrt{2}}. \tag{2}$$

In the monostatic case, where $S_{\mathrm{HV}} = S_{\mathrm{VH}}$, the Pauli matrix basis can be reduced to the first three matrices, which leads to

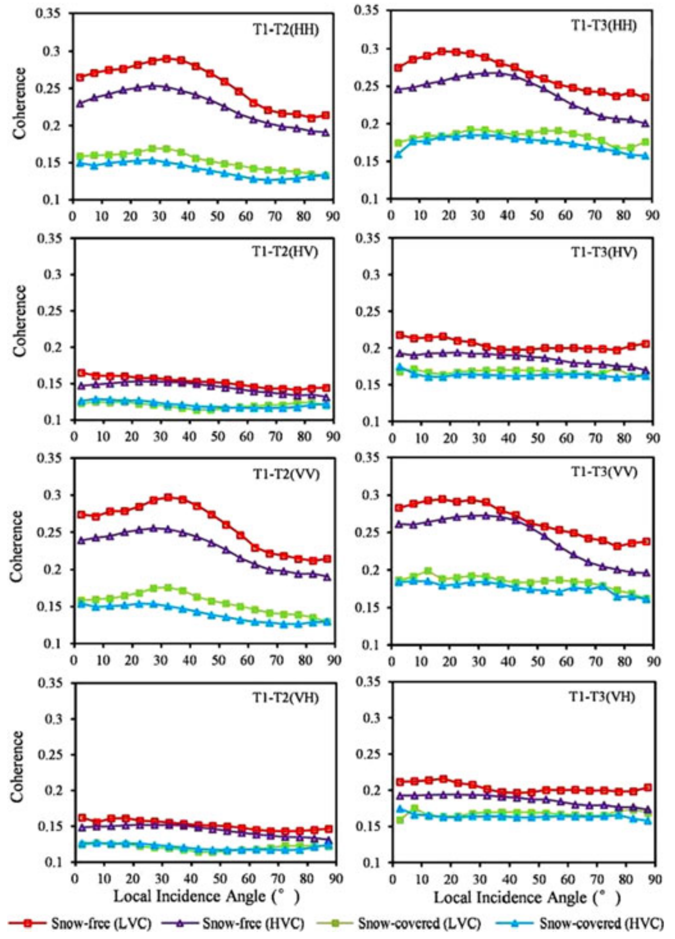

Fig. 7. Coherence value comparisons for snow-covered and snow-free pixels from HVC and LVC areas.

$d = 0$ [33]. It follows that the *Span* value is given by

$$\text{Span} = |S_{\text{HH}}|^2 + 2|S_{\text{HV}}|^2 + |S_{\text{VV}}|^2 = |a|^2 + |b|^2 + |c|^2 \tag{3}$$

where $|a|^2$, $|b|^2$, and $|c|^2$ represents the surface (Pauli_Odd), double-bounce (Pauli_Dbl), and volume scattering (Pauli_Vol), respectively. Fig. 8(c) represents the composited image of the three scattering components. A perpendicular line across the wet and dry snow cover areas is also shown in Fig. 8(c). Along the line, a typical region in mountain areas is divided into three parts using four points, A, B, C, and D. According to the field measurements and optical data, the line segment AB passes through wet snow, BC passes through mixed pixels of wet snow and bare soil, and CD passes through shallow dry snow.

As shown in Fig. 8(a), A–B represents the wet snow facies with a relatively low scattering value in double-bounce and volume scattering components, the main component of backscattering signal are snow surface backscattering from the air/snow interface at C-band [9]. The lower backscattering values during wet snow conditions are mainly due to the strong electromagnetic wave absorption of water molecules in the surface of the wet snow. When the location extends from wet snow pixels to the mixed pixels of wet snow and bare soil, scattering value of the three components increased obviously. The average scattering values of wet snow pixels was found to be 5–10 dB smaller than that of the mixed pixels in double-bounce and volume backscattering components. Average scattering values of the three components are approximately equal on B–C and C–D, and both presented significant fluctuations. This may be because that the backscattering properties of shallow dry snow at C-band are similar to that of snow-free areas. In particular, the differences of the average scattering values between dry and wet snow pixels in volume backscattering component were found to be more significant than those in surface and double-bounce scattering components. Accordingly, there is a great unrealized potential in quad-polarization SAR data for wet snow identification. Thus, we used target decomposition to find the appropriate polarimetric parameters for the classification of dry and wet snow.

D. Dynamic Thresholding Algorithm

The TSA was carried out based on the assumption that the coherence variation is only related to the changes of snow cover. The study reveal that the threshold of 0.21 and 0.20 for T1–T2 and T2–T3 coherence images, respectively, were able to achieve maximum classification accuracy of only 71.6% and 69.2% when extracting snow cover using the TSA. Since the local incidence angle and underlying surface type were considered to be closely related to coherence variation, a dynamic thresholding algorithm (DTC) was proposed, and co-polarization coherence image was applied because of the higher coherence compared with cross polarization. Based on the snow-covered and snow-free areas obtained from optical data, coherence values of selected snow-cover pixels and snow-free pixels are randomly serves as the *y*-axis, the corresponding local incidence angle of the selected pixels serves as the *x*-axis (see Fig. 9). From the distribution of the random dots, in order to classify the snow-cover pixels and snow-free pixels on different local incidence angle, a threshold should be fixed for each local incidence angle. Therefore, these optimal thresholds were calculated at an interval of 1° for each local incidence angles in the range of 0°–90°, and a thresholding line was built, as shown in Fig. 9. For each pixel of the coherence images, a threshold can be found according to its local incidence angle. Coherence value of the pixels lower than the threshold was classified as snow-covered areas. The thresholding line was built, respectively, for LVC and HVC areas.

E. Polarimetric Parameter Selection

According to the *in situ* measured data of snow wetness and snow surface temperature, snow on December 13, 2013 can be identified as dry snow, the classification for dry and wet snow are focused on the snow on March 19, 2014. It has been found that incoherent target decomposition possess the ability to obtain the desired information of snow cover from PolSAR data [13]. In this study, three commonly used incoherent target decomposition methods (*H/A/*α [27], Freeman [28], and Yamaguchi [29]), combined with Pauli decomposition, were adopted to extract appropriate polarimetric parameters for the classification of dry and wet snow.

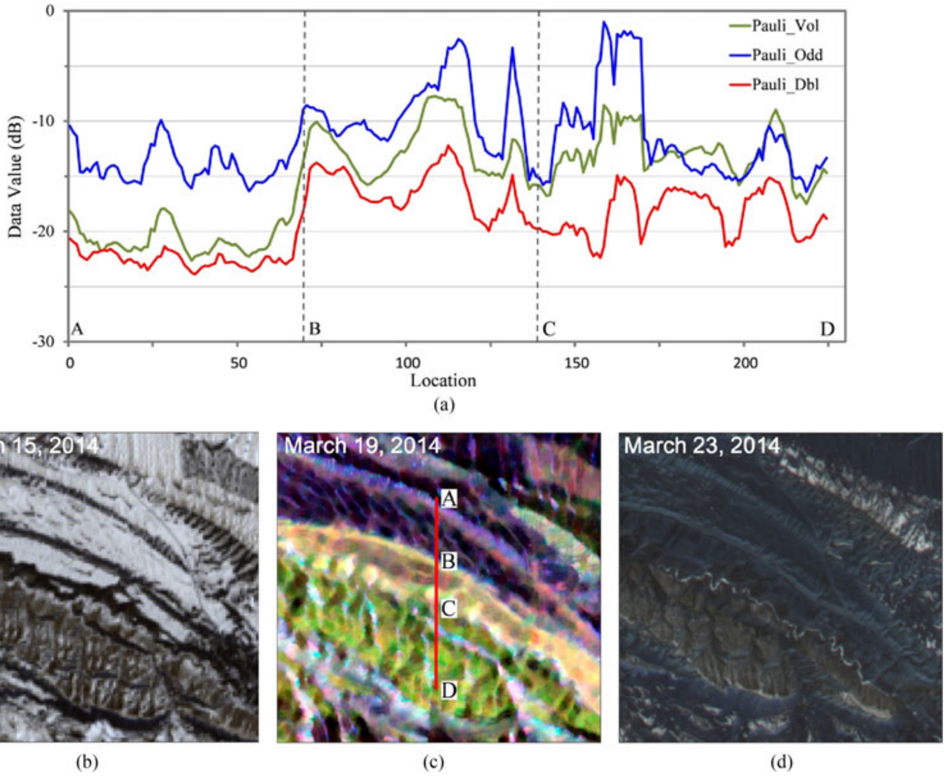

(a)

(b) (c) (d)

Fig. 8. Polarimetric information analysis. Panel (a) represents the backscattering value of Pauli decomposition results for dry and wet snow. Panel (b) represents the OLI data acquired on March 15, 2014. Panel (c) represents the composited image (R:Pauli_Dbl, G:Pauli_Vol, B:Pauli_Odd) of Pauli decomposition results acquired on March 19, 2014. Panel (d) represents the WFV data acquired on March 23, 2014. The points A–D in panel (a) corresponds to A–D in panel (c).

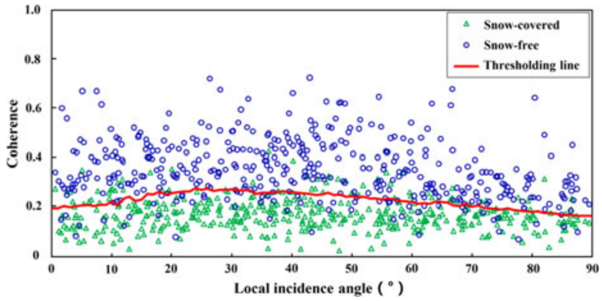

Fig. 9. Schematic diagram of dynamic thresholding algorithm.

The coherency matrix $\mathbf{T}$ is given as

$$\mathbf{T} = k \cdot k^{*T} \tag{4}$$

where $*$ and $\mathbf{T}$ represents the complex conjugate and transpose, k is a vector arranged from the backscattering matrix elements and can be expressed as follows:

$$\mathrm{k} = \frac{1}{\sqrt{2}}[\mathbf{S}_{HH} + \mathbf{S}_{VV} \;\; \mathbf{S}_{HH} - \mathbf{S}_{VV} \;\; \mathbf{S}_{HV} + \mathbf{S}_{VH}]^{\mathrm{T}}. \tag{5}$$

According to the Hermitian matrices, the coherency matrix $\mathbf{T}$ can be further expressed as follows:

$$\mathbf{T} = \left(\lambda_1 \overrightarrow{e_1}\overrightarrow{e_1}^{*\mathrm{T}}\right) + \left(\lambda_2 \overrightarrow{e_2}\overrightarrow{e_2}^{*\mathrm{T}}\right) + \left(\lambda_3 \overrightarrow{e_3}\overrightarrow{e_3}^{*\mathrm{T}}\right) \tag{6}$$

where λ_1, λ_2, and λ_3 are the three eigenvalues of $\mathbf{T}$, The *H/A/*α decomposition is based on the three eigenvalues, and defines the entropy *H,* the anisotropy *A,* and the angle $\bar{\alpha}$, which are respectively expressed as [27]

$$H = -\sum_{i=1}^{3} P_i \log 3P_i, \quad 0 < P_i = \lambda_i \left(\sum_{j=1}^{3} \lambda_j\right)^{-1} < 1 \tag{7}$$

$$A = \frac{\lambda_2 - \lambda_3}{\lambda_2 + \lambda_3}, \quad 0 \le A \le 1 \tag{8}$$

$$\bar{\alpha} = P_1\alpha_1 + P_2\alpha_2 + P_3\alpha_3, \quad 0^\circ \le \bar{\alpha} \le 90^\circ \tag{9}$$

where P_i is pseudo probability, which can be obtained from the eigenvalues. α_1, α_2, and α_3 are the eigenvector parameters.

Based on the physics of radar scattering, Freeman and Durden proposed a three-component scattering decomposition method by using a surface, volume, and double-bounce scattering mechanism [28]. According to the three-component scattering decomposition technique, the coherency matrix $\mathbf{T}$ can be expressed as follows:

$$\mathbf{T} = f_s\mathbf{T}_s + f_d\mathbf{T}_d + f_v\mathbf{T}_v \tag{10}$$

where f_s, f_d, and f_v are surface, double-bounce, and volume scatter contributions to the backscatter. Yamaguchi expanded the three-component scattering decomposition by introducing an additional term corresponding to the nonreflection symmetric case, and proposed a four-component scattering decomposition technique. According to the four-component scattering mechanism [29], the coherency matrix $\mathbf{T}$ can be decomposed

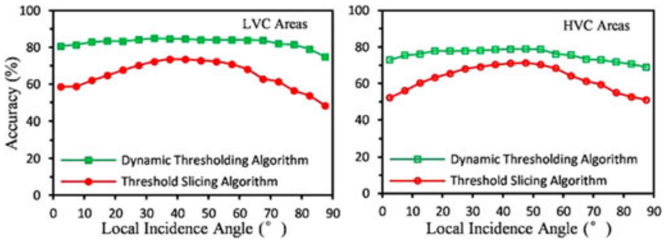

Fig. 10. Accuracy comparison for dynamic thresholding algorithm and TSA.

into

$$\mathbf{T} = f_s\mathbf{T}_s + f_d\mathbf{T}_d + f_v\mathbf{T}_v + f_c\mathbf{T}_c \tag{11}$$

where f_c is the helix scattering coefficient. $\mathbf{T}_s$, $\mathbf{T}_d$, $\mathbf{T}_v$ and $\mathbf{T}_c$ are expansion matrices corresponding to surface, double-bounce, and volume and helix scattering, respectively.

Each polarimetric parameter with its own characteristics should be used for the specific geographic object. Therefore, these parameters are analyzed to figure out which one could be used for the classification of dry and wet snow. First, Nagler algorithm [12] was used for a rough extraction of dry and wet snow, then combining with the *in situ* measured snow wetness data, dry and wet snow samples are selected and the samples are distributed as evenly as possible in the study area. Finally, Jeffreys-Matusita (J-M) distance [30] was applied for the parameter selection based on the selected samples. For the certain dry and wet snow samples, the J-M distance of the parameters can be expressed as follows:

$$\mathbf{J} = 2\left(1 - \mathrm{e}^{-B}\right), \quad 0 < \mathbf{J} < \mathbf{2} \tag{12}$$

$$B = \frac{1}{8}(m_1 - m_2)^2 \frac{2}{\delta_1^2 + \delta_2^2} + \frac{1}{2}\ln\left[\frac{\delta_1^2 + \delta_2^2}{2\delta_1\delta_2}\right] \tag{13}$$

where $\mathbf{J}$ is the J-M distance for the parameter, m_1 and m_2 are the average values of the parameter corresponding to dry and wet snow samples, $\delta_1$and δ_2 are the variance.

F. Support Vector Machine (SVM) Classification

SVM was selected for the classification due to its ability to solve nonlinear classification problems with small samples and high dimensions [31]. The SVM classifier is typically constructed based on a small number of training instance-label pairs, which are used to search for the support vectors and then to predict unknown data. For a two-class problem, it can be assumed that the training instance-label pairs are (x_i, y_i), $i = 1, \ldots, N$. Each training instance-label pair $(x_i,\, y_i)$ is a vector in the *d*-dimensional feature space $x_i = [x_{i,1},\, x_{i,2}, \ldots,\, x_{i,d}]^{\mathrm{T}}$ with a corresponding label y_i. The decision function in the kernel space can be expressed as follows:

$$f(x) = \sum_S a_i y_i K(x_i,\, x) + b \tag{14}$$

where $f(x)$ represents the margins. $S = i : 0 < a_i < C$, where C is a penalty parameter. Samples associated with nonzero a_{i} are so-called support vectors. b is a bias term that does not affect the performance significantly. $K(x_i, x)$ is the kernel function. In this study, a Gaussian radial basis function kernel was employed. This kernel took the following form [31]:

$$K(x_i,\, x) = \mathrm{e}^{-\gamma\|x_i - x\|^2} \tag{15}$$

where γ is a parameter that is inversely proportional to the width of the Gaussian kernel. The two parameters C and γ were not known beforehand, and grid-search and cross-validation methods were used to search for the best parameters [32]. Subsequently, the training instance-label pairs were used to confirm the support vectors.

In this study, there are 900 patterns from dry snow samples and 900 patterns from wet snow samples. The patterns were divided into three subsets of equal size. One subset was used to test the classifier trained on the other two subsets. After the grid search conducted using three-fold cross-validation, the best values of the two parameters were identified. Then, the classifier was finally built.

V. RESULTS AND DISCUSSION

A. Snow Cover Extraction Results

The snow cover extraction results using dynamic thresholding algorithm were validated with the optical data, considering the snow-cover and snow-free pixels from the optical data as the “ground truth” data. The results are shown in Fig. 10. Mean accuracies of the algorithm were found to be 84.2% for the LVC areas and 78.3% for the HVC areas, which are considerably higher than the 72.7% and 69.2% accuracy achieved by the TSA, respectively. In particular, the dynamic thresholding algorithm showed a more significant advantage in low incidence angle (<30°) and high incidence angle (>60°). However, the accuracy is still lower than the snow mapping accuracy of the optical data outside of shadow and cloud areas. Therefore, the final extracted snow cover is the fusion of the snow cover extraction results using the algorithm and the snow cover pixels from the optical data, based on a pixel-by-pixel confidence value.

Figure 11(a) represents the final snow cover extraction results on December 13, 2013. The optical data (December 14, 2013) corresponding to a region in Fig. 11(a) is shown in Fig. 11(b). Regions D and E in Fig. 11(a) presents, respectively, the snow cover extraction results in cloud areas and shadow areas of optical data using the dynamic thresholding algorithm. Two typical regions from LVC and HVC areas are selected, respectively, for a comparison in detail, as shown in Fig. 12. Compared with the snow cover extraction results using optical data, snow cover based on the dynamic thresholding algorithm seems extremely patchy. This may be because the coherence is affected by some other factors that cannot be accurately quantified in this study, including system thermal noise, soil moisture variations, the accuracy of DEM data, error in data processing, the activity of humans and livestock, and mixed pixel caused by the topography. On the other hand, snow cover extracted from HVC areas seems to be patchy than that of LVC areas. It may be that, underlying surface and topography of HVC areas are more complex as compared with the LVC areas, and caused a more serious decorrelation.

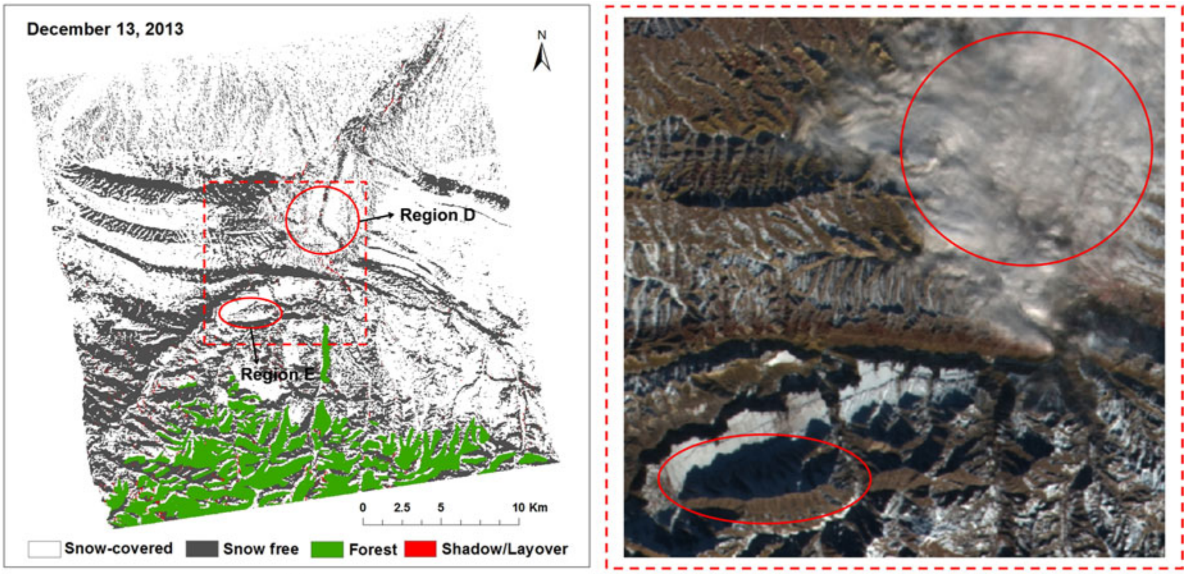

(a) (b)

Fig. 11. (a) Snow cover extraction results on December 13, 2013. (b) WFV data of GF-1 satellite with a combination of near infrared, red, and green bands acquired on December 14, 2013.

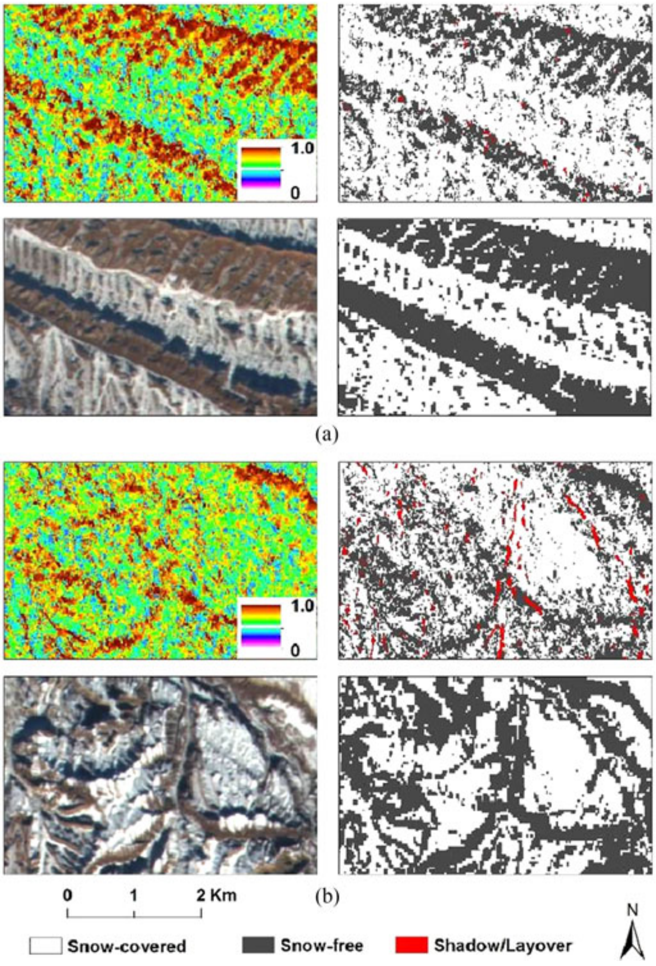

Fig. 12. Snow cover extraction results for the (a) LVC areas and the (b) HVC areas. (Top left) Coherence images. (Top right) Snow cover extraction results using the dynamic thresholding algorithm. (Bottom left) Optical data. (Bottom right) Snow cover extraction results using the optical data.

B. *Optimal Polarimetric Parameter Combination*

POLSARPRO software was used to implement the selected polarimetric decomposition methods and 36 polarimetric parameters are obtained. Detailed calculation formula and physical interpretation of the polarimetric parameter can refer to Lee and Pottier's research results [33]. We calculated the J-M distance for all the 36 polarimetric parameters, the results are shown in Table III. When the J-M distance is between 0 and 1.0, the parameter do not owns separability between dry and wet snow samples; when the J-M distance is between 1.0 and 1.8, the parameter owns a poor separability; when the J-M distance is between 1.8 and 1.9, the parameter can be used for classification only after the adjustment of the samples; and when the J-M distance is between 1.9 and 2.0, the parameter owns a good separability between dry and wet snow samples.

The results showed that the J-M distance of volume scattering component from the Pauli decomposition [P_{vol}, see Fig. 13(a)], the volume scattering component from the Yamaguchi decomposition [Y_{vol}, see Fig. 13(b)], and the third eigenvalue of the coherency matrix from the $H/A/\alpha$ decomposition [λ_3, see Fig. 13(c)] are all between 1.9 and 2.0. Therefore, the three parameters were selected as the optimal polarimetric parameter combination for the classification.

According to the *in situ* measured snow wetness data [see Fig. 13(d)], the dry snow is mainly distributed in the south of the study area, where the underlying surface is covered by subshrubs and grass. As is shown in Fig. 13(a) and (b), the dry snow (green) facies with a higher volume scattering value compared with the wet snow (blue), it mainly due to the volume scattering caused by stems of the subshrubs and grass. This means that the volume scattering component is suitable for the classification of dry and wet snow in vegetation-covered mountain areas. However, the snow-free areas have similar

TABLE III
J-M DISTANCE FOR POLARIMETRIC PARAMETERS

J-M Distance	Pauli	*H/A/*α	Yamaguchi	Freeman
0–1.0	P_{odd} (Pauli_Odd)	*(1-H)(1-A)*, *beta*, *RVI*, SE_{P}	Y_{odd} (Yamaguchi_Odd), Y_{hlx} (Yamaguchi_Hlx)	F_{odd} (Freeman_Odd)
1.0–1.8	P_{dbl} (Pauli_Dbl)	*H*, *A*, α, *HA*, λ_1, *p1*, *p2*, *T11*, *T22*, SE_{I}, *PF*, *SERD*, *DERD*, *desta*, *(1-H)A*, *SE*	Y_{dbl} (Yamaguchi_Dbl)	F_{dbl} (Freeman_Dbl)
1.8–1.9		*H(1-A)*, *p3*, λ_2, *T33*, *Span*		F_{vol} (Freeman_Vol)
1.9–2.0	P_{vol} (Pauli_Vol)	λ_3	Y_{vol} (Yamaguchi_Vol)	

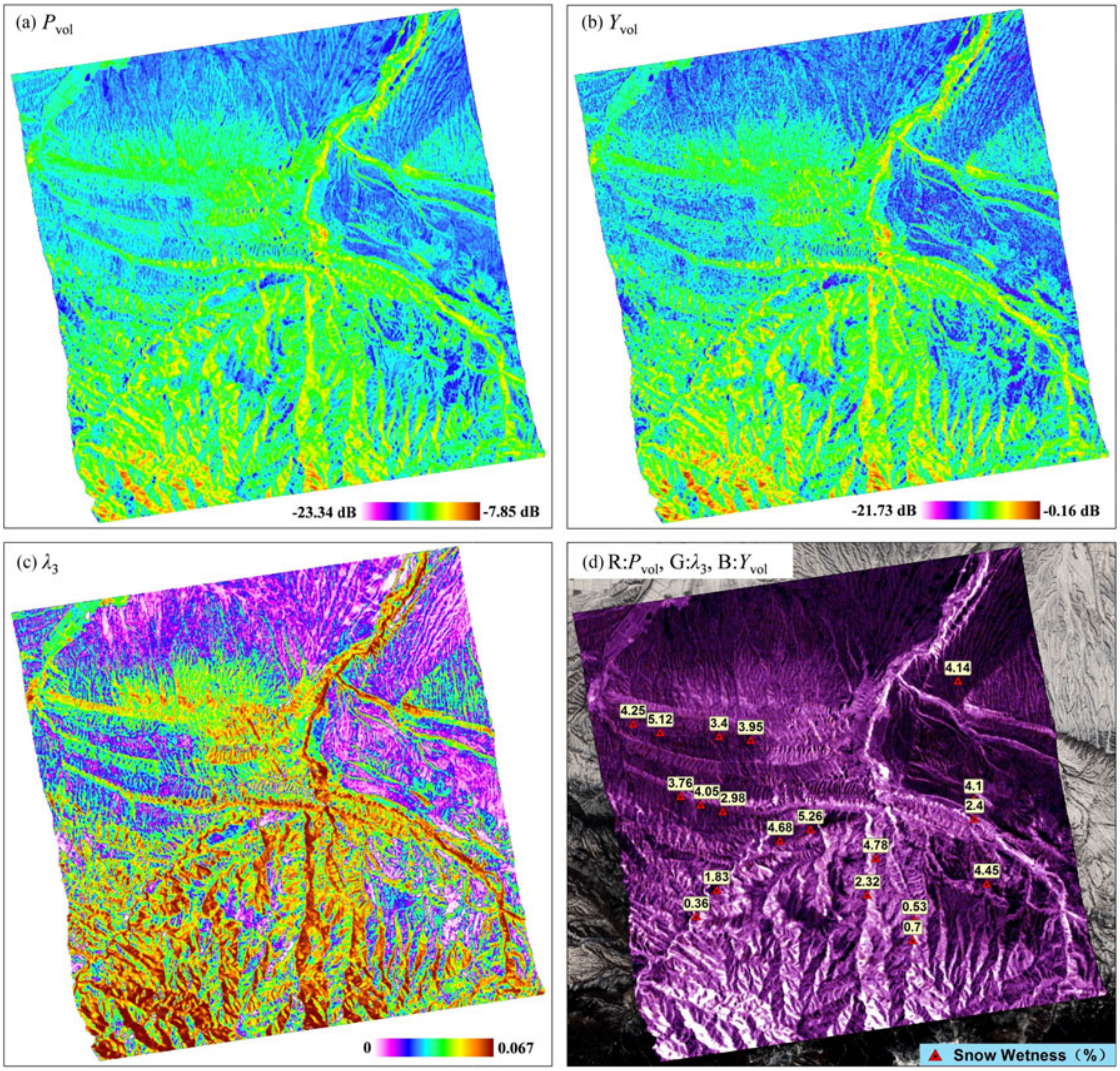

Fig. 13. Optimal polarimetric parameter combination. (a) Volume scattering component (P_{vol}) from Pauli decomposition. (b) Volume scattering component (Y_{vol}) from Yamaguchi decomposition. (c) Third eigenvalue (λ_3) of the coherency matrix from the H/A/α decomposition. (d) Composited image (R: P_{vol}, G: λ_3, B: Y_{vol}) of March 19, 2014. The background image is the OLI data acquired on March 15, 2014.

characteristics with dry-snow covered areas, both characterized by light purple in Fig. 13(d), it mainly because of the high penetration capability and low attenuation of dry snow at C-band. It is therefore difficult to distinguish between shallow dry snow and snow-free covered areas using the backscattering coefficient.

C. Dry and Wet Snow Cover Classification Results

The classifier was applied to the optimal polarimetric parameter combination and the snow cover extraction results on March 19, 2014. The classification results are presented in Fig. 14(a). The results were validated with the *in situ* data, considering the *in situ* measured snow wetness as the "ground truth" data. 31

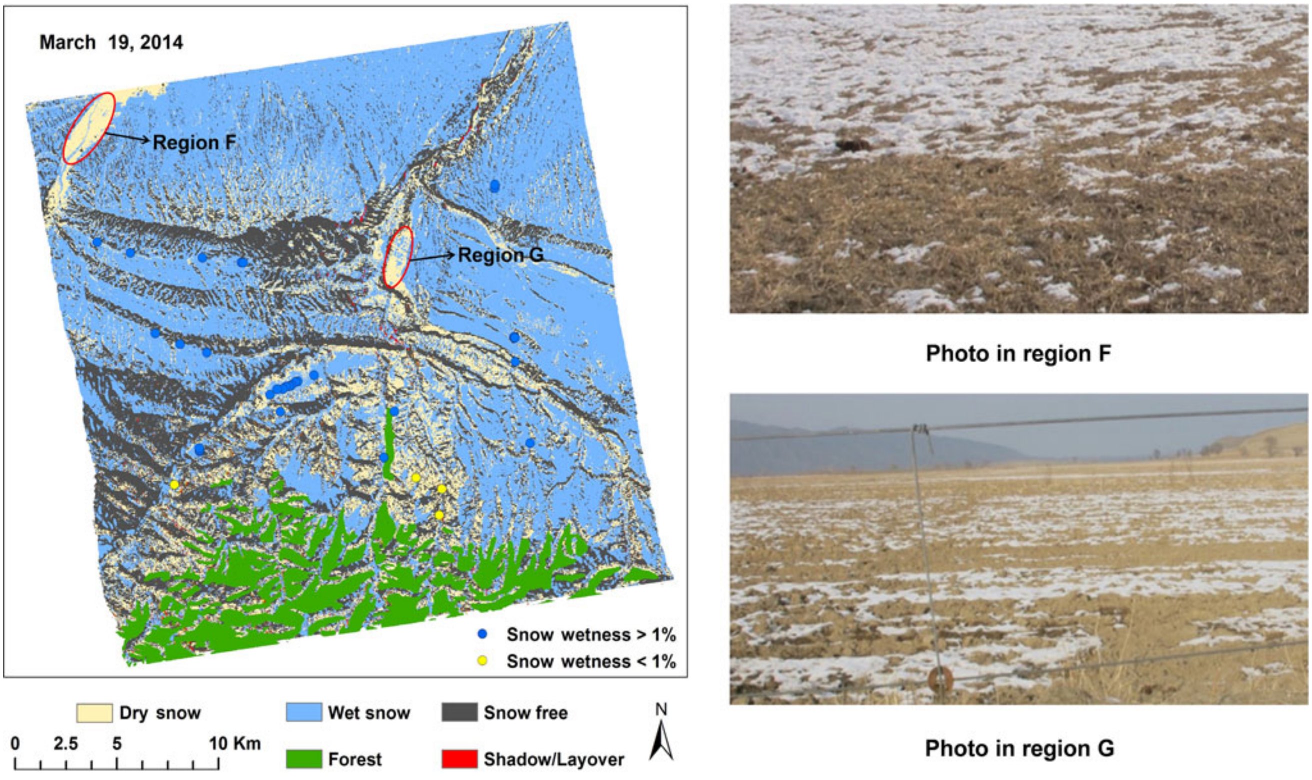

(a) (b)

Fig. 14. (a) Dry and wet snow classification results on March 19, 2014. (b) Photos taken in the site.

sample points were selected and 28 samples are in agreement with the classification results. The overall accuracy of the classification is 90.3%. Region F and region G in Fig. 14(a) are two pieces of cropland covered by the melting snow, Fig. 14(b) represents the photos taken in the site for the two regions on March 19, 2014. It can be seen that mostly snow in the two regions had melted. The remaining wet snow together with the bare soil formed the mixed pixels of the satellite data. It is noted that the two regions are both wrongly identified as wet snow cover areas, it may be that, the coherence of the two areas are relatively low, due to the decorrelation caused by the remaining wet snow and rapid increase of the soil moisture. Meanwhile, the polarization characteristics of the two areas are similar to that of the dry snow, thus leading to the misclassification using the polarimetric decomposition method.

VI. CONCLUSION

In the study, a two-step method for dry and wet snow cover identification in mountain areas was proposed based on quad-polarization SAR data and optical remote sensing data, as well as two ground-based synchronous observation experiments. First, the interferometric coherence and backscattering coefficient images of fully polarimetric RADARSAT-2 data were analyzed for the snow-accumulation period and snow-melt period, respectively, adopting snow-covered and snow-free areas obtained from GF-1 satellite observations as the "ground truth." Three factors including polarization mode, local incidence angle, and underlying surface type were found to be closely related to the coherence and been used in the proposed dynamic thresholding algorithm for snow cover extraction. Accuracy of the dynamic thresholding algorithm was found to be significantly higher than the typical TSA, especially in low and high incidence angle. Second, by using the Pauli, $H/A/\alpha$, Freeman, and Yamaguchi decomposition methods, 36 polarimetric parameters are extracted and analyzed, the results indicate that the volume scattering component from the Pauli decomposition, the third eigenvalue of the coherency matrix from the $H/A/\alpha$ decomposition, and the volume scattering component from the Yamaguchi decomposition own higher separability between dry and wet snow. These three parameters, combined with the training samples acquired from field measurements and Nagler algorithm [12], were used to build an SVM classifier to classify the extracted snow cover. The classification accuracy was verified using the *in situ* measured snow wetness. The dry and wet snow cover extraction using this method can achieve an accuracy of 90.3%. Overall, the two-step method proposed in this study offers an improved way for snow cover extraction in mountain areas by combining SAR and optical data, and also an efficient way to address the influence of snow-free areas on the classification of dry and wet snow cover.

However, the proposed method highly depends on prior knowledge obtained from *in situ* measurements and optical data, which is a general problem for supervised classification methods. Besides, some other commonly used polarimetric decomposition methods, such as VanZyl [34] and Touzi [35], need to be tested for the study area. Future work includes quantitative analysis for decorrelation in snow-covered mountain areas and polarimetric parameters. Nonetheless, the results of the study indicate a high potential of utilizing repeat-pass fully polarimetric SAR data at C-band for seasonal dry and wet snow identification in mountain areas.

ACKNOWLEDGMENT

The authors would like to thank the ESA for providing the POLSARPRO software, the USGS for the free Landsat-8 OLI data, and the anonymous reviewers for their helpful comments and suggestions.

REFERENCES

[1] S. Colbeck *et al.*, "The international classification for seasonal snow on the ground," International Association of Scientific Hydrology, vol. 253, no. 6557, pp. 743–749, 2015.

[2] T. P. Barnett, J. C. Adam, and D. P. Lettenmaier, "Potential impacts of a warming climate on water availability in snow-dominated regions," *Nature*, vol. 438, no. 7066, pp. 303–309, 2005.

[3] P. Lemke *et al.*, "Observations: Changes in snow, ice and frozen ground," *Climate Change 2007: The Physical Science Basis. Contribution of Working Group I to the Fourth Assessment Report of the Intergovernmental Panel on Climate Change*. Cambridge, U.K.: Cambridge Univ. Press, 2007, pp. 337–383.

[4] W. W. Immerzeel, P. Droogersa, S. M. de Jongb, and M. F. P. Bierkensb, "Large-scale monitoring of snow cover and runoff simulation in himalayan river basins using remote sensing," *Remote Sens. Environ.*, vol. 113, no. 1, pp. 40–49, 2009.

[5] T. C. Grenfell, S. G. Warren, and P. C. Mullen, "Reflection of solar radiation by the antarctic snow surface at ultraviolet, visible, and near-infrared wavelengths," *J. Geophys. Res.*, vol. 99, no. 9, pp. 18669–18684, 1994.

[6] D. Robinson, K. Kunzi, G. Kukla, and H. Rott, "Comparative utility of microwave and shortwave satellite data for all-weather charting of snowcover," *Nature*, vol. 312, no. 5993, pp. 434–435, Nov. 1984.

[7] J. C. Shi, Y. Du, and J. Y. Du, "Progresses on microwave remote sensing of land surface parameters," *Sci. China Earth Sci.*, vol. 55, no. 7, pp. 1052–1078, Jul. 2012.

[8] J. C. Shi, J. Dozier, and H. Rott, "Snow mapping in alpine regions with synthetic aperture radar," *IEEE Trans. Geosci. Remote Sens.*, vol. 32, no. 1, pp. 152–158, Jan. 1994.

[9] J. C. Shi and J. Dozier, "Mapping seasonal snow with SIR-C/X-SAR in mountainous areas," *Remote Sens. Environ.*, vol. 59, no. 2, pp. 294–307, Jan. 1997.

[10] T. Nagler, "Methods and analysis of SAR data from ERS-1 and X-SAR for snow and glacier applications," Ph.D. dissertation, Inst. Meteorol. Geophys., Univ. Innsbruck, Innsbruck, Austria, Sep. 1996.

[11] J. Koskinen, S. Metsämäki, J. Grandell, S. Jänne, and L. Matikainen, "Snow monitoring using radar and optical satellite data," *Remote Sens. Environ.*, vol. 69, no. 1, pp. 16–29, Jul. 1999.

[12] T. Nagler and H. Rott, "Retrieval of wet snow by means of multitemporal SAR data," *IEEE Trans. Geosci. Remote Sens.*, vol. 38, no. 2, pp. 754–765, Mar. 2000.

[13] G. Singh, G. Venkataraman, and Y. Yamaguchi, "Capability assessment of fully polarimetric ALOS-PALSAR data for discriminating wet snow from other scattering types in mountainous regions," *IEEE Trans. Geosci. Remote Sens.*, vol. 52, no. 2, pp. 1177–1196, Feb. 2014.

[14] L. Huang, Z. Li, and B. S. Tian, "Classificationand snowline detection for glacial areas using the polarimetric SAR image," *Remote Sens. Environ.*, vol. 115, no. 7, pp. 1721–1732, Jan. 2011.

[15] M. Callegari *et al.*, "A Pol-SAR analysis for alpine glacier classification and snowline altitude retrieval," *IEEE J. Sel. Topics Appl. Earth Observ. Remote Sens.*, vol. 9, no. 7, pp. 3106–3121, Jul. 2016.

[16] S. E. Park, Y. Yamaguchi, and G. Singh, "Polarimetric SAR response of snow-covered area observed by multi-temporal ALOS PALSAR fully polarimetric mode," *IEEE Trans. Geosci. Remote Sens.*, vol. 52, no. 1, pp. 329–340, Jan. 2014.

[17] F. T. Ulaby and R. K. Moore, *Microwave Remote Sensing: Active and Passive. Volume 2: Radar Remote Sensing and Surface Scattering and Emission Theory*. Reading, MA, USA: Addison-Wesley, 1982.

[18] H. A. Zebker and J. Villasensor, "Decorrelation in interferometric radar echoes," *IEEE Trans. Geosci. Remote Sens.*, vol. 30, no. 5, pp. 950–959, Sep. 1992.

[19] J. C. Shi, S. Hensleya, and J. Dozier, "Mapping snow cover with repeat pass synthetic aperture radar," in *Proc. IEEE Int. Geosci. Remote Sens. Symp.*, 1997, vol. 2, pp. 628–630.

[20] V. Kumar and G. Venkataraman, "SAR interferometric coherence analysis for snow cover mapping in the western himalayan region," *Int. J. Digit. Earth*, vol. 4, no. 1, pp. 78–90, Feb. 2011.

[21] G. J. He, P. F. Xiao, X. Z. Feng, X. L. Zhang, Z. Wang, and N. Chen. "Extracting snow cover in mountain areas based on SAR and optical data," *IEEE Geosci. Remote Sens. Lett.*, vol. 12, no. 5, pp. 1136–1140, May 2015.

[22] T. Tachikawa *et al.*, ASTER Global Digital Elevation Model Version 2-Summary of Validation Results, ASTER GDEM Validation Team. 2011. [Online]. Available: http://www.jspacesystems.or.jp/ersdac/GDEM/ver2Validation/Summary_GDEM2_validation_report_final.pdf

[23] A. Sihvola and M. Tiuri, "Snow fork for field determination of the density and wetness profiles of a snow pack," *IEEE Trans. Geosci. Remote Sens.*, vol. GE-24, no. 5, pp. 717–721, Sep. 1986.

[24] J. S. Lee, J. H. Wen, T. L. Ainsworth, K. S. Chen, and A. J. Chen, "Improved sigma filter for speckle filtering of SAR imagery," *IEEE Trans. Geosci. Remote Sens.*, vol. 47, no. 1, pp. 202–213, Jan. 2009.

[25] J. W. Rouse, R. H. Haas, J. A. Schell, and J. C. Harlan, "Monitoring the vernal advancement of retrogradation of natural vegetation," NASA/GSFC, Type III, Final Report, Greenbelt, MD, USA, p. 371, 1974.

[26] V. V. Salomonson and I. Appel, "Estimating fractional snow cover from MODIS using the normalized difference snow index," *Remote Sens. Environ.*, vol. 89, no. 3, pp. 351–360, Mar. 2004.

[27] S. Cloude and E. Pottier, "A review of target decomposition theorems in radar polarimetry," *IEEE Trans. Geosci. Remote Sens.*, vol. 34, no. 2, pp. 498–518, Mar. 1996.

[28] A. Freeman and S. L. Durden, "A three-component scattering model for polarimetricSAR data," *IEEE Trans. Geosci. Remote Sens.*, vol. 36, no. 3, pp. 936–973, Mar. 1998.

[29] Y. Yamaguchi, Y. Yajima, and H. Yamada, "A four-component decomposition of POLSAR images based on the coherency matrix," *IEEE Geosci. Remote Sens. Lett.*, vol. 3, no. 3, pp. 292–296, Jul. 2006.

[30] L. Bruzzone, F. Roli, and S. B. Serpico, "An extension of the Jeffreys-Matusita distance to multiclass cases for feature selection," *IEEE Trans. Geosci. Remote Sens.*, vol. 33, no. 6, pp. 1318–1321, Nov. 1995.

[31] G. V. Camps and L. Bruzzone, "Kernel-based methods for hyperspectral image classification," *IEEE Trans. Geosci. Remote Sens.*, vol. 43, no. 6, pp. 1351–1362, Jun. 2005.

[32] Y. Bazi and F. Melgani, "Toward an optimal SVM classification system for hyperspectral remote sensing images," *IEEE Trans. Geosci. Remote Sens.*, vol. 44, no. 11, pp. 3374–3385, Nov. 2006.

[33] J. S. Lee and E. Pottier, *Polarimetric Radar Imaging: From Basics to Applications*. Boca Raton, FL, USA: CRC Press, 2009, pp. 214–262.

[34] J. J. Van Zyl, H. Zebker, and C. Elachi, "Imaging radar polarization signatures: Theory and application," *Radio Sci.*, vol. 22, no. 4, pp. 529–543, 1987.

[35] R. Touzi, "Target scattering decomposition in terms of roll-invariant target parameters," *IEEE Trans. Geosci. Remote Sens.*, vol. 45, no. 1, pp. 73–84, Jan. 2007.

Guangjun He was born in Hubei, China, in 1987. He received the B.S. degree in geographic information system from Yangtze University, Jingzhou, China, in 2009, the M.S. degree in cartography and geographic information system from Fujian Normal University, Fuzhou, China, in 2012, and the Ph.D. degree in remote sensing of environment from Nanjing University, Nanjing, China, in 2015.

Since 2015, he has been a Research Associate in the State Key Laboratory of Space-Ground Integrated Information Technology, CAST, Beijing, China. He is the author of more than ten articles. His research interests include multi-sensor information fusion, remote sensing of snow, and remote sensing image processing.

Xuezhi Feng was born in Gansu, China, in 1953. He received the B.S. degree in cartography from Nanjing University, Nanjing, China, in 1979.

From 1980 to 1981, he was a Lecturer in the Department of Geography, Nanjing University. Then, he was with the Lanzhou Institute of Glaciology and Cryopedology, Chinese Academy of Sciences, as an Assistant Professor from 1981 to 1990, as an Associate Professor from 1990 to 1994, as a Professor from 1994 to 1997. Since 1997, he has been a Professor in the Department of Geographic Information Science, Nanjing University. He is the author of four books and more than 200 articles. His research interests include remote sensing of snow and remote sensing image processing.

Pengfeng Xiao (M'13) was born in Hunan, China, in 1979. He received the B.S. degree in land resource management from the Hunan Normal University, Changsha, China, in 2004, and the Ph.D. degree in cartography and geographical information system from Nanjing University, Nanjing, China, in 2007.

From 2007 to 2009, he was a Lecturer in the Department of Geographic Information Science, Nanjing University, where he has been an Associate Professor since 2010. He is the author of two books and more than 50 articles. His research interests include remote sensing image segmentation, land use and land cover change, and remote sensing of snow.

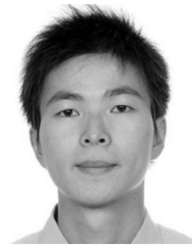

Zhenghuan Xia was born in Jiangxi, China, in 1986. He received the Ph.D. degree in electromagnetic field and microwave technology from Institute of Electronics, Chinese Academy of Sciences, Beijing, China, in 2015.

Since 2015, he has been with the State Key Laboratory of Space-Ground Integrated Information Technology, CAST, Beijing, China. His current research interests include novel spaceborne synthetic aperture radar system, UWB radar system, and remote sensing image processing.

Zuo Wang was born Anhui, China, in 1988. He received the B.S. degree in geographical information system from Anhui Normal University, Wuhu, China, in 2008, the M.S. degree in cartography and geographical information system from Fujian Normal University, Fuzhou, China, in 2011, and the Ph.D. degree in cartography and geographical information system from Nanjing University, Nanjing, China, in 2014.

Since 2014, he has been a Lecturer in the Anhui Normal University. He is the author of more than ten articles. His research interests include remote sensing of snow and radiometric calibration of sensor.

Hao Chen was born in Gansu, China, in 1988. He received the B.E. degree in communication engineering from the University of Bath, Bath, U.K., in 2011, and the M.S. degree in electronic and communication engineering and network from the University of Birmingham, Birmingham, U.K., in 2015.

He is currently working with the State Key Laboratory of Space-Ground Integrated Information Technology, CAST, Beijing, China. His research interests include object detection and speech recognition by using the artificial neural networks.

Hui Li was born in Hubei, China, in 1985. She received the B.S. degree in geographical information system from North East Normal University, Changchun, China, in 2007, and the Ph.D. degree in remote sensing of environment from Nanjing University, Nanjing, China, in 2012.

Since 2012, she has been the Lecturer in the Department of Spatial Information Science and Engineering, Xiamen University of technology, Xiamen, China. She is the author of more than ten articles. Her research interests include remote sensing of snow and remote sensing image processing.

Jinjin Guo was born in Shandong, China, in 1989. She received the B.S. degree in geographical information system from the Shandong Jianzhu University, Ji'nan, China, in 2012, and the M.S. degree in cartography and geographical information system from Nanjing University, Nanjing, China, in 2016.

She is the author of one article. Her research interests include snow cover recognition and SAR polarization decomposition.